



HAL
open science

An EAM potential for α -brass copper–zinc alloys: application to plasticity and fracture

Antoine Clement, Thierry Auger

► **To cite this version:**

Antoine Clement, Thierry Auger. An EAM potential for α -brass copper–zinc alloys: application to plasticity and fracture. *Modelling and Simulation in Materials Science and Engineering*, 2022, 31 (1), pp.015004. 10.1088/1361-651X/aca4ec . hal-04072754

HAL Id: hal-04072754

<https://cnam.hal.science/hal-04072754>

Submitted on 26 Nov 2023

HAL is a multi-disciplinary open access archive for the deposit and dissemination of scientific research documents, whether they are published or not. The documents may come from teaching and research institutions in France or abroad, or from public or private research centers.

L'archive ouverte pluridisciplinaire **HAL**, est destinée au dépôt et à la diffusion de documents scientifiques de niveau recherche, publiés ou non, émanant des établissements d'enseignement et de recherche français ou étrangers, des laboratoires publics ou privés.

Copyright

An EAM potential for α -brass copper–zinc alloys: application to plasticity and fracture

Antoine Clement and Thierry Auger* 

PIMM, Arts et Métiers Institute of technology, CNRS, CNAM, HESAM Université,
151 Bd de l'hôpital, 75013 Paris, France

E-mail: thierry.auger@ensam.eu

Received 1 September 2022; revised 27 October 2022

Accepted for publication 22 November 2022

Published 9 December 2022

Abstract

An embedded atom method potential has been developed for copper–zinc alloys valid from 0% to 37% zinc content (dedicated to describe the α fcc phase). It has been fit to a set of first-principles data for the fcc copper, the fcc Cu_3Zn DO_{23} phase and Zn on a fcc lattice. Elastic anisotropies, the lattice parameter, cohesive energy are used as input. Punctual defects, surface energies, intrinsic stacking fault and phonon spectrum have been computed and compare well with experimental trends. This potential has been used to study dislocation dissociation and dislocation emission at a crack tip up to 30% Zn. Dislocation emission at the crack tip is correctly described compared with recent parametrization including the surface energy. It is found that with alloying, dislocation emission becomes easier following the decrease of the unstable stacking fault energy with Zn concentration, a non-trivial finding. This potential is therefore well suited to carry out basic studies of plasticity and fracture in α -brass alloys.

Keywords: embedded atom method, copper alloys, dislocation emission, generalized stacking fault energy

(Some figures may appear in colour only in the online journal)

1. Introduction

Among the copper rich binary alloys, merely nine of them show significant solubility in the solid state face centred cubic α -phase at room temperature (one considers those with a threshold notably above a few at%). These stable solid solution alloys are Cu–Al, Cu–Au, Cu–Ga, Cu–Ge, Cu–Li, Cu–Mn, Cu–Pd, Cu–Pt and Cu–Zn. The other possible binaries can be classified either as metastable alloys (Cu–Ni, Cu–Zr or Cu–Sn for example) or are immiscible to a large extend (Cu–Ag, Cu–W or Cu–Pb for example) [1]. Among the ‘highly soluble’

* Author to whom any correspondence should be addressed.

couples, Cu–Au, Cu–Pd and Cu–Pt alloys serve as a test bed for order-disorder phase transition studies given that the entire composition domain falls on a fcc type lattice. Embedded atom method (EAM) potentials have indeed been developed for these systems since the early time of use of this approach [2–4]. This is eased first by the fact that the alloying elements of these later couples have also a fcc structural ground state, and second because the fcc ground state is stable over the entire composition range. In order to reasonably describe these alloys from a thermodynamical point of view the different ordered phases are then usually included in the potential development (leaving out the issue of a correct short range order description). A common functional form for the interaction cutoff, which is highly desirable for modelling an alloy [5], can then be defined.

Out of the six remaining, Cu–Zn brass alloys stand out as being particularly interesting being a widely used structural materials or a model system for environmental fracture (stress corrosion cracking and liquid metal embrittlement [6–8]) and plasticity [9]. A major challenge is that the ground state of Zn is hcp with a c/a ratio of 1.856. The definition of a suitable EAM potential for a hcp element cannot be achieved if the c/a ratio is above the ideal packing ratio $\sqrt{8/3} \sim 1.63$ [10]. The Cu–Zn system is also a classical example with Hume-Rothery phases whose shifts in structural lattice ground states are driven by the valence electron/atom ratio (inducing α , β , γ and then ϵ phases). Therefore it is probably out of reach to develop an EAM potential describing such type of alloy over the entire range of composition because the EAM framework does not address this particular alloying physics. Nevertheless, one would still like to be able to carry out plasticity and fracture study via an atomistic type modelling, a goal one can achieve by restricting the description to the α solid solution range (the fcc ground state) thereby relaxing the constraint on the hcp zinc ground state and replacing it with a fcc one.

This would add to the currently available set of EAM potentials for fcc alloys (Al–Mg or Ni–Al [11, 12]) that has become popular to study solid solution hardening for concentrated alloys [13, 14]. This is highly desirable as these two systems have the drawback of a limited solubility (respectively 5 at% and 15 at%). Using the Cu–Zn system, one can explore and compare with experiment in an extended composition range up to nearly 37% without dealing with intermetallic formation in a different structural ground state (one notes that other solid solution binaries such as Cu–Al or Cu–Ga systems have a cc beta phase above 20%). Being a model alloy where experimental data on basic mechanical properties such as critical resolved shear stress (CRSS) are available at low temperature, α -brass is therefore an interesting target for EAM modelling of mechanical properties.

In order to proceed with Zn within the EAM framework as an alloying element in copper, it is paramount to choose not to describe its hcp ground state but to choose a fcc one, fitted on density functional theory (DFT) results, as this has already been done for a Mg–Al–Zn alloy MEAM potential [10]. This choice restricts the domain range in the binary phase diagram where the potential matches experiment and should be used (0–37 at% in this case). An intrinsic value of this approach is then that by fitting the potential relative to DFT computed properties (here for copper, then the $D0_{23}$ compound of Cu_3Zn and fcc Zn), it enables the potential to be easily used within a quantum mechanical/molecular modelling (QM/MM) framework. Elastic coupling corrections are then minimized at the domain’s interface with the necessarily smaller quantum domain. The goal of this article is therefore to report on the definition of such an EAM potential for the Cu–Zn binary system in the alpha-brass range paving the way to studies of plasticity and fracture issues in these fcc alloys over a large composition range.

As an application of using the potential about to be described, the edge dislocation properties and the dislocation emission process at the crack tip of Cu–Zn alloys is investigated in this work and confronted to the Peierls-Nabarro gamma surface theory as developed by Rice

[15], then Sun and Beltz [16] and recently adapted by Andric and Curtin [17] with the surface effects for the emission of a heading partial Shockley dislocation at a crack tip. The behaviour of the crystal is studied by computing the critical stress intensity factors (SIFs) for dislocation emission (K_{Ie}) and fracture (K_{Ic}) with both theory and simulations. The brittle fracture versus dislocation emission processes at the crack tip of Cu–Zn alloys are then compared in an anisotropic elastic setup following the classical approach of the brittle versus ductile behaviour. The results show that a ductile behaviour is predicted at 0 K in good agreement with existing experimental data at 4.2 K. The potential is then validated to be able to capture correctly the physics for both plastic and fracture behaviour and paves the way to modelling ductile as well as environmental fracture potentially also within a mixed quantum mechanics/molecular mechanics approaches (QM/MM) framework.

2. Cu–Zn EAM potential

2.1. EAM framework

The EAM framework for interatomic potential was originally developed by Daw and Baskes [18]. The total energy of the crystal computed with EAM is composed of a pair-wise term and an effective mean field embedding term emulating multi-body interactions that depends on the local electronic density created by the surrounding atomic environment. The EAM total energy then reads:

$$E = \sum_i F_i(\rho_i) + \frac{1}{2} \sum_{(i,j), i \neq j} \phi_{ij}(r_{ij}) \quad (1)$$

with $\phi_{ij}(r_{ij})$ the two-body interaction term for two atoms at a distance r_{ij} within a maximum interaction range (taken here to include up to the fifth fcc shell) and $F_i(\rho_i)$ the embedding energy function of atom i at the electronic density ρ_i on the corresponding atomic site (the sum i runs over all atoms of the crystal). The electronic density felt at a given site i is computed by the superposition of electronic densities set by neighbouring atoms. It is expressed as:

$$\rho_i = \sum_{j, j \neq i} f_j(r_{ij}) \quad (2)$$

with $f_j(r_{ij})$ the electronic density induced by an atom j at a distance r_{ij} from site i within the maximum interaction range. Following Daw and Baskes [18], the electronic density function also depends on the type of atom j which contributes to the electronic cloud. For an alloy A–B, three functions ($\phi_{t,t}$, f_t , F_t), $t \in \{a, b\}$ are needed for each element (A, B) as well as a cross-function for the interaction between A and B. The approach developed by Wadley *et al* [5] for the EAM potential of fcc alloys is followed here: in order to deal with alloys an element type specific cutoff distance (also called normalized cutoff) is used. The pair interaction function is a modified Morse potential with a short-range repulsive term and a long-range attractive one. The electronic density function is rescaled from the long-range part of the pair interaction term. The two first functions then reads:

$$\phi_{t,t}(r) = \frac{Ae^{-\alpha\left(\frac{r}{r_e^t}-1\right)}}{1 + \left(\frac{r}{r_e^t} - \kappa\right)^{20}} - \frac{Be^{-\beta\left(\frac{r}{r_e^t}-1\right)}}{1 + \left(\frac{r}{r_e^t} - \lambda\right)^{20}} \quad (3)$$

$$f_t(r) = \frac{f_e^t e^{-\beta\left(\frac{r}{r_e^t}-1\right)}}{1 + \left(\frac{r}{r_e^t} - \lambda\right)^{20}}, \quad t \in \{a, b\}. \quad (4)$$

In these functions (3) and (4), $A, B, \alpha, \beta, \kappa, \lambda$ are adjustable parameters set for each element (the t index has been dropped for clarity). κ and λ define the element's specific normalized cutoff. The constant r_e^t is set to the distance to the first neighbour fcc shell (depending on the element's type $t \in \{a, b\}$), f_e^t is the ratio of the element's cohesive energy and a characteristic atomic distance ($f_e^t = \frac{E_c^t}{\Omega_t^{1/3}}$ with Ω_t the atomic volume of the pure element and $t \in \{a, b\}$).

The embedding energy function is defined following Barnerjea and Smith [19] so that it reproduces the universal binding-electron relation energy for high electronic density (or equivalently for smaller distance between atoms). Close to the equilibrium electronic density however and for the long range interaction, a third order polynomial development of the deviation from the equilibrium density is used instead to avoid known issues with the pressure dependence of the bulk modulus [5]. The piecewise embedding function therefore reads:

$$F_t(\rho) = \begin{cases} \sum_{l=0}^3 F_{nl}^t \left(\frac{\rho}{\rho_n} - 1 \right)^l & \text{for } \rho < \rho_n \text{ with } \rho_n = 0.85\rho_e^t \text{ (long range part)} \\ \sum_{l=0}^3 F_l^t \left(\frac{\rho}{\rho_e} - 1 \right)^l & \text{for } \rho_n \leq \rho < \rho_0 \text{ with } \rho_0 = 1.15\rho_e^t \text{ (near equilibrium)} \\ F_e^t \left[1 - \ln\left(\frac{\rho}{\rho_e}\right)^{\eta^t} \right] \left(\frac{\rho}{\rho_e} \right)^{\eta^t} & \text{for } \rho_0 \leq \rho \text{ (repulsive core)} \end{cases} \quad (5)$$

Here F_e^t, η^t, F_{nl}^t and the F_l^t are adjustable parameters sets of the polynomials for each element ($t \in \{a, b\}$). ρ_e^t is the equilibrium electronic density (214.2 eV nm⁻¹ for copper, 68.4 eV nm⁻¹ for zinc, evaluated from DFT). The three forms are to be matched at the density junctions in value, slope and concavity to yield a completely smooth embedding function thus defining a set of constraints on the parameter fit.

An established procedure for defining the EAM interaction term for the alloying part relies on the observation that one can keep the EAM energy invariant upon a linear shift in density affecting both the pair-wise and the embedding terms [20, 21]. It can be shown that enforcing this invariance leads to the following functional form for the cross-function [20]:

$$\phi_{a,b}(r) = \frac{1}{2} \left[\frac{f_b(r)}{f_a(r)} \phi_{a,a}(r) + \frac{f_a(r)}{f_b(r)} \phi_{b,b}(r) \right]. \quad (6)$$

However, this parameter cross-function did not give satisfying results for the ordered Cu₃Zn compound used to fit the potential in α -brass Cu-Zn alloys for the cohesive energy and the lattice parameter. Indeed, the equilibrium lattice parameter for $L1_2$ ordering would be found at 0.3781 nm and 0.3777 for $D0_{23}$ ordering for our best trial, when DFT-GGA computations give respectively 0.3684 and 0.3683 nm. The cohesive energy would also be largely off with respectively -2.720 and -2.723 eV atom⁻¹ instead of the DFT-GGA value of -3.140 and -3.142 eV atom⁻¹. Since this invariant condition is not mandatory, the choice was made instead to use a slightly different mixing term following Gola and Pastewka [22]:

$$\phi_{a,b}(r) = \alpha_a \phi_{a,a}(r) + \alpha_b \phi_{b,b}(r). \quad (7)$$

The function is still a linear combination of $\phi_{a,a}$ and $\phi_{b,b}$ but with constants coefficients α_a and α_b . The $L1_2$ lattice is a fcc ordering where one site is occupied by one type of atom and the three other sites by an other type of atom as shown on figure 1(a). The $D0_{23}$ lattice is a $L1_2$ type ordering combined with an antiphase boundary every 2 unit cells as seen on figure 1(b), where black atoms are substitutional elements (here zinc) and white atoms are the matrix ones (here copper). It was studied by Turchi *et al* [23] in a Korringa-Kohn-Rostoker-Coherent Potential Approximation *ab-initio* pair-interaction approach and by Müller and Zunger [24] by DFT within the LDA approximation. Both approach differ for long range ordering of Cu₃Zn (Müller and Zunger [24], the ground state is a $D0_{23}$ ordering whereas for Turchi *et al* [23] it is a $L1_2$). The question of the Cu₃Zn ground state is investigated here within the DFT-GGA

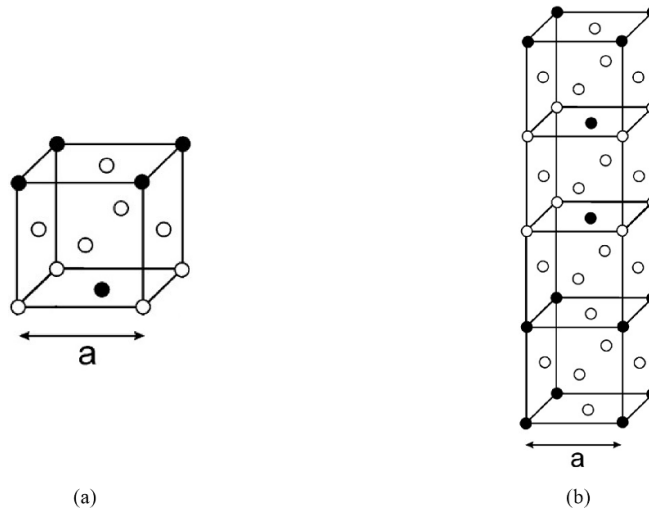


Figure 1. Cu_3Zn unit cells: (a) $L1_2$ long range ordering. (b) DO_{23} long range ordering.

approximation. As a result the DO_{23} defined compound at 25% is chosen (Cu_3Zn) as will be shown in a later part.

The next step in the potential setup procedure is to fit the EAM model parameters on desired target properties. Being mostly interested in mechanical properties, the lattice parameters, the cohesive energies, the elastic anisotropies, the bulk modulus and the vacancy formation energies were chosen. For copper the energy difference between the fcc ground state and the hcp state as well as the hcp lattice parameter were selected as well. These two constraints were found crucial if one is to describe reasonably the stacking fault energy of copper. Concerning zinc, the choice is made here to fit the potential on a fcc rather than a hcp ground state. This obviously induces a strong limitation on the zinc potential as it is only suitable for zinc in solid solution in a fcc solvent. As there is of course no experimental data on fcc zinc, one has to rely entirely on *ab-initio* computations by DFT for the properties of the elements. This implies that we give herein a new DFT-GGA fitted EAM potential for copper along with one usable for copper–zinc alpha brass alloys only.

We are unaware of a pre-existing EAM copper potential fitted on DFT-GGA, therefore it was deemed interesting to develop a new one compared with existing copper EAM potentials in view of using it within a QM/MM framework for plasticity and fracture modelling. Such a potential for copper and copper–zinc fcc alloys therefore opens the way to multi-scale modelling with this model material for various processes (with the restriction of using DFT-GGA for the QM part).

3. EAM potential fitting procedure

3.1. *Ab-initio* calculations

The *ab-initio* calculations required for the two pure elements and the ordered Cu_3Zn , DO_{23} compound included in the fit were performed using VASP software (version 5.4) [25–28]. For both copper and zinc, a GGA/PBE [29, 30] approximation for the exchange and correlation energy was used with the PAW [31, 32] pseudo-potentials provided by VASP (with respectively

Table 1. DFT Lattice parameters and cohesive energy for $D0_{23}$ and $L1_2$ ordering.

Ordering	Lattice parameter (nm)	Cohesive energy (eV atom ⁻¹)	Formation enthalpy (meV atom ⁻¹)
$D0_{23}$	0.3683	-3.142	-73.5
$L1_2$	0.3684	-3.140	-71.5

11 and 12 valence electrons). A 700 eV energy cutoff was used in all calculations. The lattice parameter of each element were converged relative to the number of k-points in reciprocal space using a Monkhorst-Pack grid of $15 \times 15 \times 15$ points sampling throughout all structural calculations. The properties computed using VASP are the lattice parameter, the cohesive energy, the anisotropic elastic constants (C_{11} , C_{12} , C_{44}), the bulk modulus, the vacancy formation energy for both copper and zinc while the hcp lattice parameter and the energy difference between hcp and fcc were computed only for copper. The elastic constant were obtained via the second derivative of the energy of a crystal while straining it around its equilibrium position using VASP.

For fcc zinc, DFT calculations result in a negative C_{44} . This can be explained by the fact that DFT does not predict fcc for the ground state of zinc and that a shear deformation of a cubic cell would drive the unstable fcc cell towards the hcp symmetry. The C_{44} from DFT for zinc on a fcc lattice was therefore not used as target in the EAM potential fit.

The long range ordered $L1_2$ and $D0_{23}$ crystals of alpha-brass alloy with 25% of zinc were computed within DFT to study the equilibrium lattice parameter, the cohesive energy and the formation enthalpy. For $L1_2$, a $15 \times 15 \times 15$ k-points grid was still used while a $24 \times 24 \times 6$ k-points grid was used for $D0_{23}$. The results are reported in table 1.

The cell used for the $D0_{23}$ is a $L1_2$ chemical ordering with an antiphase boundary every 2 unit cells for a total of 36 atoms as seen on figure 1(b). The equilibrium lattice parameter and the cohesive energy of the 25% Zn alloy are found respectively at 0.3683 nm and -3.142 eV atom⁻¹. As can be seen in table 1, the $D0_{23}$ ordering presents a lower formation enthalpy than the $L1_2$ one. This results is in agreement with LDA results obtained by Müller and Zunger [24]. With LDA, the formation enthalpy is found at -88.1 meV atom⁻¹ for $D0_{23}$ and -87.4 meV atom⁻¹ for $L1_2$. There is a difference of 0.7 meV atom⁻¹ for LDA with the $D0_{23}$ ordering as the fundamental state. With GGA, the difference is of 2 meV atom⁻¹, with also the $D0_{23}$ ordering as the ground state. This justifies here that the $D0_{23}$ ordering for Cu_3Zn alloy is being used as a target for the cross-term in the EAM potential.

In addition to the afore mentioned properties to be used as target in the fit, surface energetics and interstitials formation energetics were calculated to serve as a test bed for the EAM potential prediction. Surface energies (111), (110) and (100) were computed using a $1 \times 1 \times 12$ supercell (respectively $0.257 \times 0.445 \times 3.1$, $0.3635 \times 0.257 \times 4.96$ and $0.3635 \times 0.3635 \times 3.635$ nm³) with respectively 24, 24 and 42 atoms. The vacuum in the supercell along the surfaces normal is set to 1 nm. The three layers closer to the surface were relaxed while the ones at the centre of the bulk were kept fixed at the equilibrium lattice parameter. The relaxation criterion was set to 0.01 meV for the cell energy. The k-points mesh was a $15 \times 15 \times 1$ automatic Monkhorst-Pack grid (with 1 k-point along the surface's normal direction).

3.2. EAM potential constraints

To determine the thirty four parameters of the EAM functional, the following fitting procedure described was pursued:

- When developing their different potentials, Wadley *et al* [5] found out that some parameters follow strict relationships for every potential. We applied, for each of their potentials, the following two constraints: $\alpha = 1.875 * \beta$ and $\lambda = 2 * \kappa$. They also set F_i^l to 0 for every potential they developed. This comes from the need to keep a symmetric curve in compression or in tension around the equilibrium density, relegating anharmonic effect as a third order correction. These relations were implemented in the optimization algorithm (this reduces the number of independent parameters to only 28).
- Constraints on the piecewise embedding energy function were initially set to impose continuity on the embedding function, its first and second derivatives (slope and concavity). An additional constraint comes from the requirement to have no interaction at infinity. Deriving these constraints on the two junctions of the three piecewise embedding function results in the following seven equations:

$$\left\{ \begin{array}{l} F_0 = F_e * (1 - \eta * \ln(1.15)) * 1.15^\eta - F_2 * 0.0225 - F_3 * 0.003375 \text{ (continuity)} \\ 0.3 * F_2 = -F_e * \eta^2 * 1.15^{\eta-1} * \ln(1.15) - 3 * F_3 * 1.15^2 \text{ (1st derivative continuity)} \\ F_3 = \frac{F_e * \eta^2}{0.45} * 1.15^{\eta-2} * (\ln(1.15) * (\frac{1.15}{0.15} - \eta + 1) - 1) \text{ (2nd derivative continuity)} \\ F_{n0} = F_0 + 0.0225 * F_2 - 0.003375 * F_3 \text{ (continuity)} \\ F_{n1} = 0.85 * (-0.3 * F_2 + 0.0675 * F_3) \text{ (1st derivative continuity)} \\ F_{n2} = 0.7225 * (F_2 - 0.45 * F_3) \text{ (2nd derivative continuity)} \\ F_{n3} = F_{n0} + F_{n2} - F_{n1} \text{ (no interaction at } \infty) \end{array} \right. \quad (8)$$

- The target function to minimize was defined as a weighted mean-square error function between the physical constant calculated in DFT and the same characteristic calculated with the EAM potential to be optimized. This function was then first minimized using a simplex algorithm (the Nelder-Mead algorithm [33]). The weights of the target function were then adjusted so as to constraint the algorithm to converge priorily on the least accurate part of the potential. This two-step process was iterated until the algorithm reached a minimum for the χ_2 function. A total of a few tens of iterations (around 50) was enough to obtain a reasonable fit.

The constraints on the piecewise embedding function could however not all be simultaneously fulfilled strictly. To cope with this issue, the constraint derived from the continuity of the second derivative ($F_3 = \frac{F_e * \eta^2}{0.45} * 1.15^{\eta-2} * (\ln(1.15) * (\frac{1.15}{0.15} - \eta + 1) - 1)$) of the embedding energy function was removed. For copper and zinc, there is therefore a cusp at $\rho = 1.15\rho_e$ with a mismatch of the second derivative of 0.145 eV for Cu and 0.125 eV at high density in the embedding term. The fact that this condition is not satisfied will trigger odd behaviour of the potential only at extremely large compression which is deemed not important in the context of our planned applications of these potentials for plasticity and fracture.

The best fit for the parameters found with this procedure for the EAM potential is given in table 2. The potential fitting procedure was made with a builtin cutoff of 2.5 times the highest lattice parameter (2.5×0.3935 nm). To choose this cutoff, we compute every contribution of the neighbouring atoms and no longer take it into account when the contribution is deemed negligible (roughly less than 2 meV atom⁻¹). This corresponds to approximately five neighbouring shells.

At last, the cross-term function (equation (7)) parameters were fitted with a simple minimization algorithm (Nelder-Mead [33]) to the cohesive energy and lattice parameter of the $D0_{23}$ ordered state of Cu₃Zn compound. The objective function was computed as a simple

Table 2. Parameters for copper and zinc for the EAM potential (F_1 set to 0) for both element.

Parameters	Copper	Zinc
α	9.891 407	5.949 160
β	5.275 417	3.171 034
A (eV)	0.256 897	0.221 878
B (eV)	0.418 186	0.248 483
κ	0.433 274	0.406 005
λ	0.866 547	0.811 215
F_{n0} (eV)	-2.508 147	-0.482 090
F_{n1} (eV)	-0.098 405	-0.260 091
F_{n2} (eV)	0.276 606	0.725 983
F_{n3} (eV)	-2.133 136	0.503 984
F_0 (eV)	-2.516 853	-0.505 153
F_2 (eV)	0.388 957	1.035 112
F_3 (eV)	0.013 583	0.067 316
F_e (eV)	-2.513	-0.485
η	0.439 728	0.811 336

mean-square error function. The parameters obtained by this procedure are $\alpha_a = 0.89502$ and $\alpha_b = 0.39372$.

The potential files were produced using the ase framework [34] as interpolated spline tables.

3.3. EAM potential basics computations

The potentials are used in this section to first predict interstitial formation energy and surfaces energies. The results from these EAM calculations and their counterparts computed by DFT are presented in table 3 along the physical quantities used in the fit.

One can note that apart from the hcp-fcc energy difference for copper and the vacancy formation energy for zinc, the lattice parameter, cohesive energy, elastic anisotropy, bulk modulus and vacancy formation energy reported in table 3 are well fitted relative to the *Ab-Initio* computations (less than 1%). Even if there is a mismatch for the energy difference between hcp and fcc, the difference is large enough to ensure that the crystal does not transform too easily into a hcp state upon straining. For copper, the correct ordering of surface energies as predicted by DFT ($\gamma_{(111)} < \gamma_{(100)} < \gamma_{(110)}$) is obtained with this EAM potential. For zinc, the (111) surface energy is too high as already mentioned and the ordering of surface energy between (100) and (110) is not correct. The EAM framework is not particularly suited for reproducing them, a MEAM (Modified EAM) potential that takes into account an angular term would perform better as used by Dickel *et al* [10]. The lattice parameter, cohesive energy, elastic anisotropy and bulk modulus for alpha-brass with 25% of zinc were computed with the EAM potential and DFT. A DO_{23} fully ordered alloys was setup on a fcc basis cell with 36 atoms (27 of copper and 9 of zinc) as shown on figure 1(b) with a size of $0.3683 \times 0.3683 \times 1.4732 \text{ nm}^3$. A $L1_2$ ordered alloy cell as seen on figure 1(a) was also used with a size of $0.3684 \times 0.3684 \times 0.3684 \text{ nm}^3$. The elastic properties were computed both by DFT and with the EAM potential. For the latter scheme, 1000 different random configurations at the equilibrium lattice size were generated to simulate a random alloy with a $10 \times 10 \times 10$ lattice cell (about $4 \times 4 \times 4 \text{ nm}^3$) and the results for computed physical properties were averaged. The results from these calculations and their DFT counterparts, when calculated, are presented in table 4. Since the DO_{23} ordering presents

Table 3. Results of DFT-GGA with PAW calculations for copper and zinc. The one used for the fitting of the potential are grayed. The others are predictions.

Physical Characteristics	Copper		Zinc	
	DFT	EAM	DFT	EAM
Lattice parameter (nm)	0.3635	0.3634	0.3935	0.3935
Cohesive energy (eV atom ⁻¹)	-3.729	-3.719	-1.087	-1.087
C_{11} (GPa)	180.5	180.9	138	138
C_{12} (GPa)	119.7	120.0	82.9	82.9
C_{44} (GPa)	83.36	83.57	-3.36	35.9
Bulk modulus (GPa)	140.0	140.3	101	101
Vacancy formation energy (eV)	1.216	1.206	0.602	0.547
Lattice parameter hcp (nm)	0.2558	0.2570	0.2615	0.274
Energy difference hcp-fcc (eV atom ⁻¹)	0.010	0.005	-0.223	0.015
Surface energy (111) (mJ m ⁻²)	1295	1097	486	801
Surface energy (110) (mJ m ⁻²)	1536	1329	730	840
Surface energy (100) (mJ m ⁻²)	1444	1201	879	802
Interstitial formation energy (eV)	3.67	3.30	1.50	1.25

Table 4. Results of DFT-GGA with PAW computations for Cu₃Zn alpha-brass (fcc) and their matching EAM values. The ones used for fitting of the potential are coloured in gray. The others are EAM predictions.

Physical Characteristics	Cu ₃ Zn alpha-brass alloy				
	DFT-GGA (D0 ₂₃)	DFT-GGA (L1 ₂)	EAM (D0 ₂₃)	EAM (L1 ₂)	EAM (Random alloy)
a_0 (nm)	0.3683	0.3684	0.3684	0.3685	0.3683
E_C (eV at ⁻¹)	-3.1416	-3.1400	-3.1257	-3.1244	-3.1235
ΔH_f (eV at ⁻¹)	-0.0735	-0.0715	-0.0647	-0.0634	-0.0625
C_{11} (GPa)	157 (157)	158	180.4 (181.7)	181.7	152.6
C_{12} (GPa)	116 (115)	120	126.7 (127.3)	125.6	103.7
C_{44} (GPa)	74.1 (74.8)	74.8	71.09 (70.71)	71.40	67.27
B (GPa)	130	132	144.9	144.3	120.0

a loss of symmetry in the c direction, the elastic constants are different in that direction. The values for this direction are presented in parenthesis in table 4.

The lattice parameter for the D0₂₃ fully ordered Cu₃Zn alpha-brass is well reproduced and the corresponding DFT cohesive energy is matched by EAM within 1%. The EAM potential reproduces well the D0₂₃ ground state compared to the L1₂ long range ordering. The EAM predictions for the anisotropic elastic constants of the ordered alloy Cu₃Zn as well as the bulk modulus are predicted within 5% of their DFT values except for the C_{11} value (see table 4). This matching level for the elastic anisotropies is deemed sufficient for the potential to be useful in elasto-plastic modelling.

Table 5. Comparison for copper: DFT, this work, Mishin and Foiles potentials, experiments.

	DFT-GGA	EAM this work (0 K)	Experiment (0 K) [36]	Experiment (300 K) [36]	Mishin <i>et al</i> [3]	Foiles <i>et al</i> [35]
a_0 (nm)	0.3635	0.3635	0.3602 [37]	0.361	0.3615	0.3615
E_C (eV at ⁻¹)	-3.729	-3.719		-3.49	-3.54	-3.54
B (GPa)	140.0	140.3	142	137	138.3	138.5
C_{11} (GPa)	180.5	180.9	176.2	168.4	169.9	167.3
C_{12} (GPa)	119.7	120.0	124.9	121.4	122.6	124.2
C_{44} (GPa)	83.36	83.57	81.8	75.4	76.2	76.45

3.4. Pure copper: comparison with other potentials

The potential developed here for copper is compared to other already available ones (Mishin *et al* [3] and Foiles *et al* [35]). DFT and EAM computations from this work and experimental results at 0 K [36] are reported in table 5 for the lattice parameter, the cohesive energy and the elastic constants. While, of course, the new proposed EAM potential is within 1% of the DFT results, the Mishin *et al* [3] and Foiles *et al* [35] potentials significantly diverge for the lattice parameter, the cohesive energy and the C_{44} elastic constant. This is not surprising since these potentials were developed to reproduce the measured experimental quantities at room temperature. The experimental values at 300 K do indeed compare well with their predictions for these two potentials as can be seen in table 5. It is known that DFT-GGA approximation underbinds, a lattice parameter greater with GGA calculations than with experience is logically found. As already stated, the EAM potential reproduces well the elastic constants obtained with DFT-GGA calculations and in addition it also compares well with the 0 K experimental results [36].

The phonon spectrum for copper was also computed at various point in the Brillouin cell with the new EAM potential to be compared to previous DFT computations [38]. It was computed using the Phonon library from ASE [34], using the small displacement method as implemented by Alfè [39]. As can be seen on figure 2, the EAM and experimental phonon spectra at 80 K from [40] match reasonably well. It implies that this new EAM potential can be used with confidence in molecular dynamics at low finite temperature.

3.5. CuZn- α alloys: lattice parameter and mixing enthalpy

The lattice parameter and the mixing enthalpy evolution with the zinc concentration have been computed for the alpha-brasses up to 35% of zinc. It was computed using LAMMPS framework [41] with 100 supercells of $10 \times 10 \times 10$ fcc cells at fixed concentration but random configurations. Each supercell was relaxed down until convergence. The lattice parameter and the mixing enthalpy for each concentration were then averaged.

The mixing enthalpy is negative all the way to 35% of zinc in the alloy as shown in figure 3. It shows as expected from the phase diagram that the EAM Cu-Zn potential predicts a stable solid solution for the alpha-brass alloys. That is in agreement with experiment and the DFT computations of Muller and Zunger for Cu_3Zn [24]. As seen on figure 3, the $D0_{23}$ is the lowest energy state of 25% zinc alloys in DFT calculations relative to a random alloy. Long range ordering is therefore more favourable. Moreover, the results obtained with the new potential

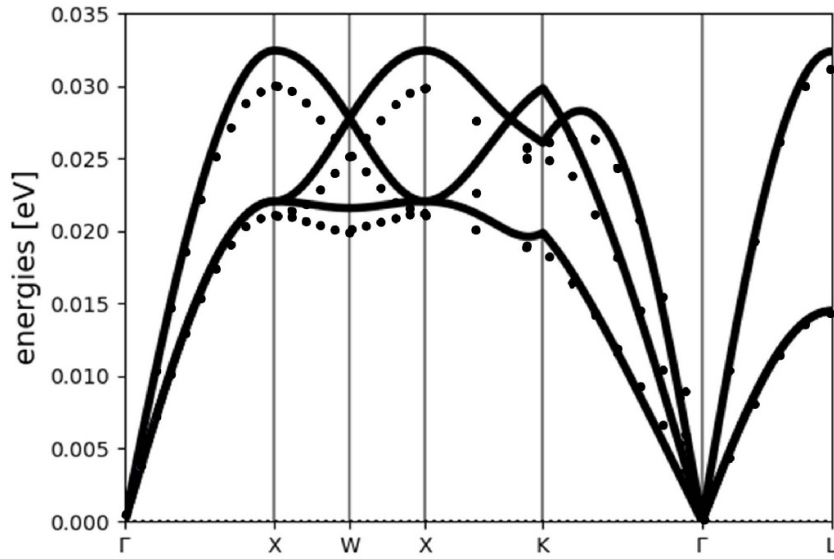


Figure 2. Phonon Spectrum computed in EAM (black lines) and experimental spectrum at 80 K (black dots).

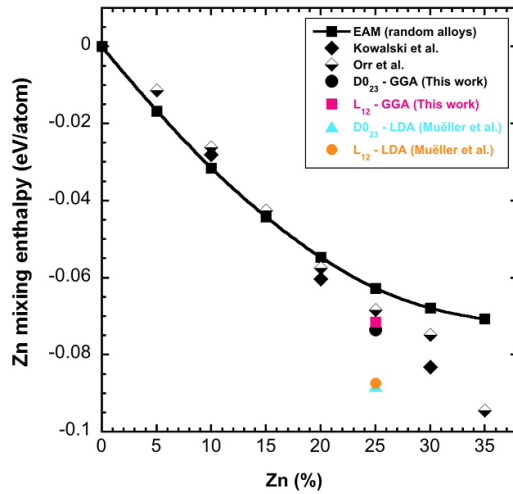


Figure 3. Mixing enthalpy as a function of zinc concentration.

follows well the one from previous *ab-initio* results [23, 24] as well as experimental ones [42, 43] along all the concentration range.

The lattice parameter evolution as a function of the zinc concentration is shown in figure 4. One can note that it almost follows a Vegard's law (linearly mixing law). According to Rao experiments [44], the α -brass lattice parameter follows a Vegard's law with a slight deviation already noticed by Johnson *et al* [45] for brasses. The agreement is nevertheless within 1%.

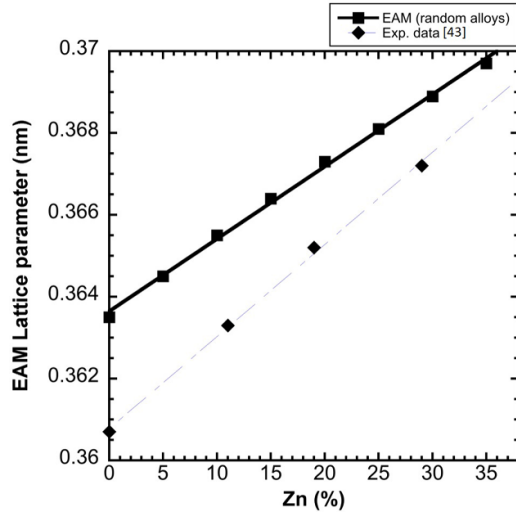


Figure 4. Lattice parameter (at 0 K for EAM and 4.2 K for texperimental [44]) as a function of zinc concentration.

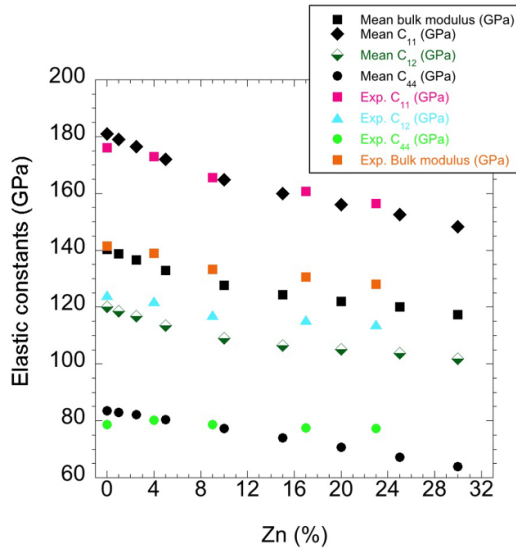


Figure 5. Elastic Constants depending on the concentration of zinc in an alpha-brass alloy [46].

3.6. CuZn- α alloys: elastic constants

Anisotropic elastic properties for the α -brass alloys depending on zinc concentration were studied with the new EAM potential. The cubic anisotropic elastic constants (C_{11} , C_{12} , C_{44}) and the bulk modulus were computed at 0 K by averaging over a thousand random configurations for each zinc concentrations. The measured experimental values at 4.2 K [46] are also reported on figure 5. The results are consistent with the experimental ones at low zinc

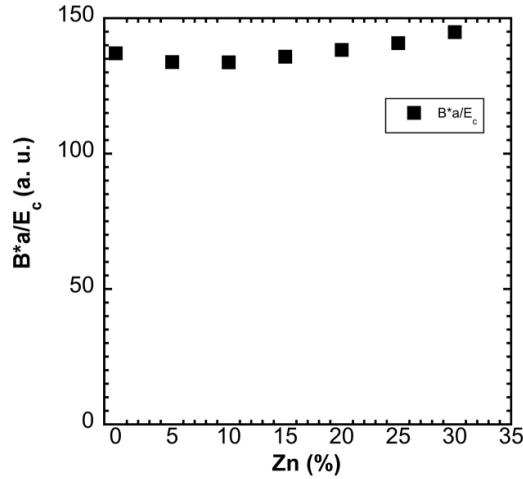


Figure 6. Ratio $\frac{B(c)*a(c)}{E_c(c)}$ depending on the concentration of zinc in an α -brass alloy.

concentration. A slight discrepancy (around 10%) occurs mostly for C_{12} for the largest zinc content. Overall, one observes a decrease of elastic constants with increasing zinc concentration consistent with the increase in lattice parameter mimicking the experimental trend. The decrease of elastic constants with the concentration is indicative of the elastic softening of the crystal when substituting copper with zinc.

According to Pettifor [47] the band filling physics of cohesion for 3d elements implies that the ratio $\frac{B(c)*a(c)}{E_c(c)}$ with B the bulk modulus, a the lattice parameter and E_c the cohesive energy should be a constant. Figure 6 provides this ratio as a function of zinc concentration. One can observe that this rule is nearly followed as a function of zinc concentration using our new potential indicating interestingly that our mixing scheme of EAM captures qualitatively well this trait of 3d elements bonding.

4. Study of the edge dislocation in Cu–Zn alloys

As an application of the use of the new EAM potential in copper–zinc α -alloys, a detailed study of the edge dislocation is presented here. The first step is a characterization of the different stacking fault energies along with the equilibrium dissociation length. Second, the Peierls stress will also be evaluated for copper. A comparison with DFT results for the edge dislocation in copper is carried out when available from the literature.

4.1. Stacking fault energies

In a fcc crystal, a perfect edge dislocation dissociates in two Shockley partial dislocations ($\frac{1}{2}\langle 110 \rangle \rightarrow \frac{1}{6}\langle 11\bar{2} \rangle + \frac{1}{6}\langle 112 \rangle$). Between these two partial dislocations, a stacking fault forms which size is controlled by the stacking fault energetics. Upon shearing along a burgers vector in the $\langle 112 \rangle$ direction, the head partial dislocation experiences an energy barrier to overcome: the unstable stacking fault (USF) energy from which one can extract the Peierls stress. In order to compute the different stacking fault energies, a shear displacement up to a Burger’s vector is imposed on a single crystal along the corresponding direction: $\langle 112 \rangle$ for USF and intrinsic stacking fault (ISF) and $\langle 110 \rangle$ for generalized stacking fault. Mapping

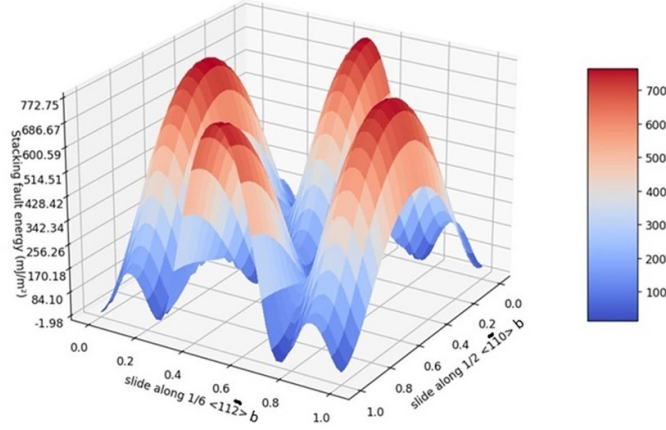


Figure 7. Stacking fault energy map depending on displacement along $\langle 110 \rangle$ and $\langle 112 \rangle$ directions.

displacements in both directions, a generalized γ surface can be computed and is presented in figure 7. Different barriers can be seen on this figure. Along the $\langle 112 \rangle$ direction, there are two barriers: the first one correspond to the USF energy, for the creation of a dissociated Shockley dislocation along $\langle 112 \rangle$. The first minimum along that direction corresponds to the ISF which is the energy of the stacking fault induced by half a burgers vector displacement. The curve in figure 8, which corresponds to the variation of energy of a fully relaxed crystal when its upper-half is displaced by a fraction of the Burgers vector, compares the energy barrier computed with EAM, DFT and results found with previously available potentials for copper [3] [48]. The sheared crystal is relaxed down to 10^{-10} eV at each step with a conjugate-gradient algorithm with the LAMMPS MD code. Results for both the unstable and ISF are compared to *ab-initio* computations and experimental results found in the literature [3, 48–51].

Concerning copper, the EAM potential matches closely the DFT curve obtained by Wu *et al* [51] except when the displacement reaches a burger’s vector for the ISF energy (28 mJ m^{-2} for the EAM potential and 43 mJ m^{-2} for DFT results). Previous potentials [3, 48] were closer to experimental (respectively 44 and 47 mJ m^{-2} compared to 40 mJ m^{-2} [49, 50]) as seen on figure 8. The USF (governing dislocation emission) is nevertheless well reproduced (175 mJ m^{-2} by DFT for Wu *et al* [51], 177 mJ m^{-2} for this work, 158 mJ m^{-2} by EAM for Mishin *et al* [3] and 184 mJ m^{-2} by EAM for Li *et al* [48]). When an ISF is created, an hcp stacking plane appears instead of a fcc plane. Its energy creation depends then partly on the energy difference between fcc and hcp. It is then no surprise that the results are not in line with the DFT results since, as seen on table 3, the energy difference between fcc and hcp with the newly developed EAM potential is far off by 30%. However, this difference in USF energy will mostly affect the dissociation length and has limited effect on the emission process.

Concerning the α -brass alloys, the drop in ISF is not predicted to be as steep than the one experiment measures. We note that the EAM potential for zinc gives a positive hcp-fcc energy difference (table 3) which might not favour lowering ISF at high zinc concentrations as much as required to match closely experiment. The prospect of performing better for this physical quantity might lie into the inclusion of the zinc hcp ground state that would be a challenge for EAM type potential.

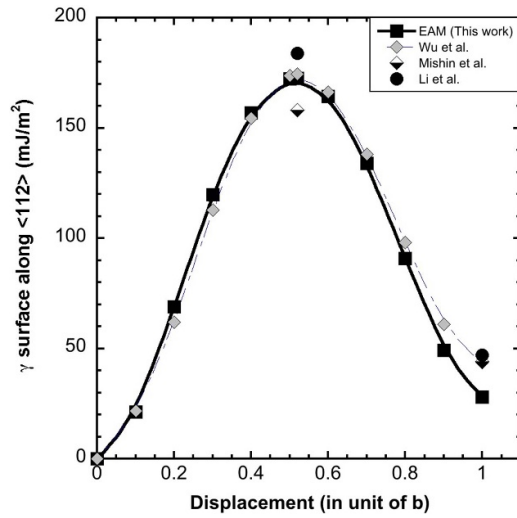


Figure 8. Comparison of stacking fault energy in EAM, DFT and literature [3, 48].

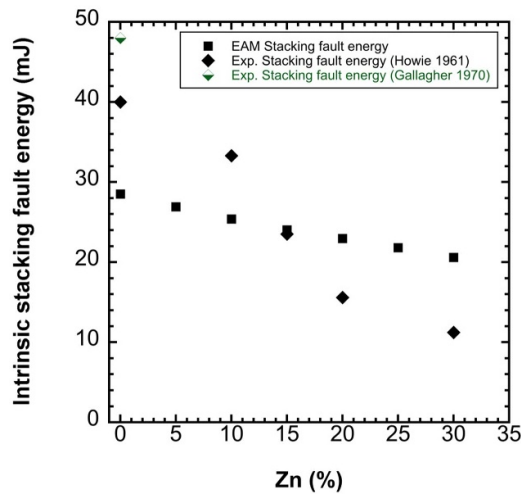


Figure 9. ISF energy depending on zinc concentration.

The ISF for α -brass as a function of zinc concentration is presented thereafter. To deal with configurational changes in the solid solution, the results of 100 different configurations were averaged to smooth the effect of fluctuations of local concentration. The results were compared to experimental results by Howie and Swann [49] and Gallagher [50] (for the ISF). The experimental trend for the ISF as a function of Zn concentration is a marked decrease by a factor of 4. The EAM potential predicts also a significant decrease of the ISF as the concentration of zinc increases (figure 9). While for copper there is a 25% lower value for the ISF, the ones predicted for the CuZn alloys are higher at the highest zinc concentration.

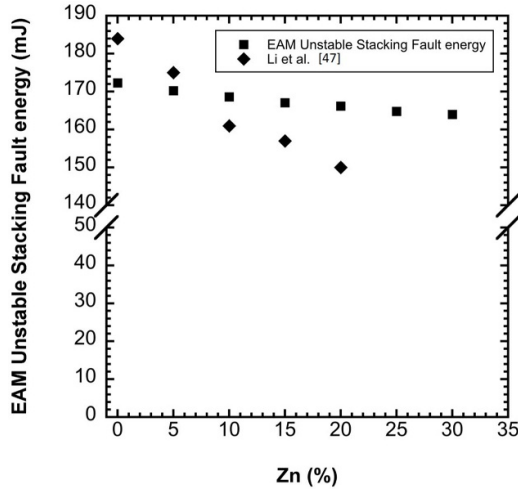


Figure 10. USF energy depending on zinc concentration compared with *ab-initio* EMTO results [48].

The results for USF energies were also compared to previous results in the literature [48] (*ab-initio* EMTO) on figure 10. As already stated, the results of the EAM potential compare well with the *ab-initio* results for the USF energy for copper. For α -brass, the USF values obtained were averaged over 100 configurations as for the ISF. The trend is similar to the one for ISF energy: the energy is decreasing with the addition of zinc in the alloy. As seen on figure 10, the values compares well to the estimate by *ab-initio* EMTO (Exact Muffin-Tin Orbital) of Li *et al* [48]. Since the USF energy drives the dislocation emission at a crack tip, one can infer that the potential would give a trend close to the behaviour that *ab-initio* EMTO calculation would predict albeit with a significantly lower slope.

4.2. Dissociation length of dislocations

The ISF energy is linked to the dissociation length of a perfect dislocation into two partial Shockley dislocations ($(\frac{1}{2}\langle 110 \rangle \rightarrow \frac{1}{6}\langle 11\bar{2} \rangle + \frac{1}{6}\langle 112 \rangle$ in fcc). Indeed, the linear elastic theory relates the dissociation distance to the inverse of the ISF energy [52]. Since the new potential reproduces well the ISF energy of the CuZn alloy, one should have reliable predictions of the distance of dissociation as well.

In order to study the dissociation length of the edge dislocation, a perfect $\langle 110 \rangle$ dislocation was introduced in an α -brass crystal of dimension $25 \times 60 \times 45 \text{ nm}^3$ with the axis along $\langle 1\bar{1}0 \rangle$, $\langle 111 \rangle$ and $\langle 11\bar{2} \rangle$ with a given zinc concentration in a random configuration. This crystal was relaxed at 0 K and the dislocation partial line adopts a wavy shape thereby minimizing energetic cost at the core figure 11. The distance of dissociation of the resulting partial dislocations was computed by averaging along the transverse direction. As seen in figure 12, the dissociation distance increases with the zinc concentration and correlates with the decrease of the ISF energy. Moreover, the distance obtained was compared to previous literature results [53, 54] and with the elastic theory. The result with the new potential fits very closely with Aslanides and Pontikis [54] results for copper. The dissociation distance lying at 5.2 nm for both potentials. One note that both predicted distances are higher than the experimentally measured one

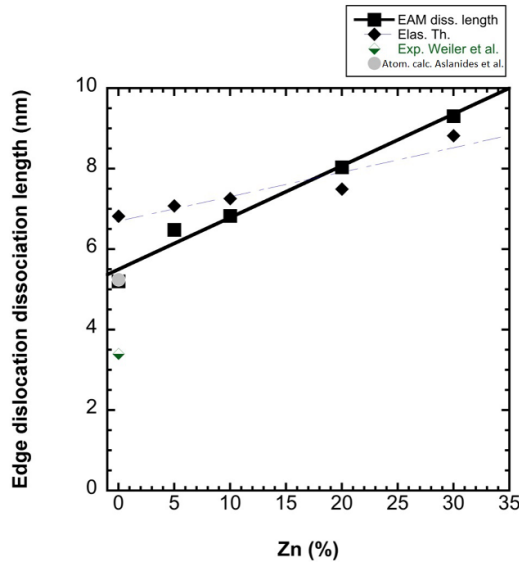


Figure 11. Dislocation dissociation length in α -brass depending on zinc concentration.

[53]. When adding the alloying effect, the dissociation distance is close to the one computed from elastic theory incorporating the ISF as given in Hirth and Lothe [52].

4.3. Peierls stress for copper

The Peierls stress for copper was computed with the new potential. It is the stress needed for a dislocation to begin to move in its glide plane. It is usually computed at 0 K. The Peierls stress was taken as the shear stress needed to move a Shockley partial dislocation by one Burger's vector. The box used to study the Peierls stress was a $25 \times 30 \times 4 \text{ nm}^3$ box with the axis along $\langle 1\bar{1}0 \rangle$, $\langle 111 \rangle$ and $\langle 11\bar{2} \rangle$ directions. The dislocation moved in the $(\langle 1\bar{1}0 \rangle, \langle 11\bar{2} \rangle)$ plane and its line was along the $\langle 11\bar{2} \rangle$ direction. The size of the box along the $\langle 11\bar{2} \rangle$ axis was increased until the results no longer depended on the box size. The crystal containing the dislocations was sheared with increasing displacement of the external atom layers along $\langle 11\bar{2} \rangle$ for the upper part and along $\langle \bar{1}\bar{1}2 \rangle$ for the lower part. The resulting stress in the crystal was computed using the virial stress implemented in LAMMPS and the Peierls stress was equated to the one reached when the dislocation moved from one Peierls valley to the next one. The critical stress is read at 0.3 MPa. This estimate is close to the experimental extrapolation at 0 K by Kamimura *et al* [55].

5. Application to dislocation emission at a crack tip in CuZn α -alloys

A study of dislocation emission at crack tip is presented here. This work is devoted to the impact of the alloying element on dislocation emission. The dislocation emission will be compared with Peierls-Nabarro theoretical modelling of dislocation emission [16, 17] and with Griffith fracture [56].

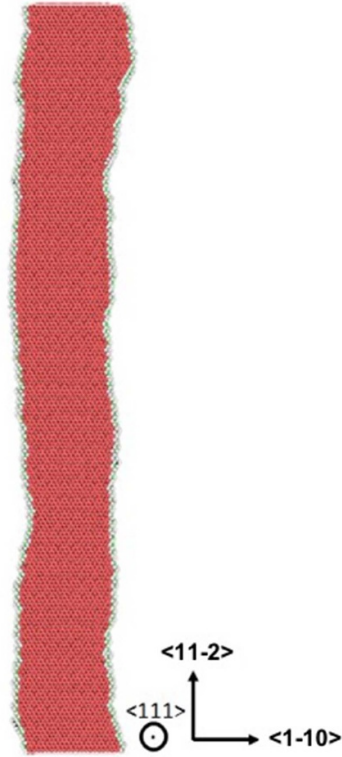


Figure 12. Wavy dislocation stacking fault for a relaxed configuration in a 5% α -brass.

5.1. Methodology

A parallelepipedon monocrystal with $\langle 1\bar{1}0 \rangle$, $\langle 111 \rangle$ and $\langle 11\bar{2} \rangle$ axis is used in this study. Periodic boundaries are applied along the transverse $\langle 11\bar{2} \rangle$ direction. To create the crack tip, the same procedure as Andric and Curtin [17] was followed. Three atomic (111) layers were deleted across half of the crystal. The crack plane was chosen to contain the surface of lowest energy (for copper (111)). The simulated box has a transverse thickness of 2 nm for pure copper but a much larger in-plane size so that one may qualify it as a quasi-2D modelling setup. As one is interested in dislocation emission with a well defined SIF in an anisotropic setup, it is important to apply confined plasticity boundary conditions on the simulation box. The crystal was strained with confined plasticity conditions at the crack tip imposed by a anisotropic displacement boundary conditions contour for a mode I loading state (see appendix A for a detailed derivation). This contour is shown on figure 13 where it is labelled boundary conditions zone. In order to be able to follow multiple dislocation emission events and to fully capture intermediate states, a large in-plane box is required. Moreover, the box has to be large enough to suppress unwanted surfaces interactions at the crack tip. Due to the mode I stress concentration at the crack tip, a dislocation after emission will move in an inclined (111) plane until the local applied shear stress falls below the Peierls stress of 0.3 MPa (see previous section). This defines a dislocation free zone (DFZ) whose size defines the minimum simulation box size that

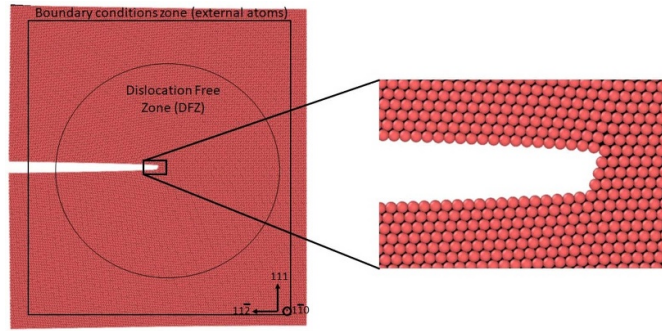


Figure 13. Cracked cell of copper for the simulation of dislocation emission at crack tip with details of the crack tip configuration.

will be taken. The size of the DFZ was computed with elastic theory in anisotropic media [57] (resolved shear component lower than the Peierls threshold) and reads about 20 nm for pure copper. The simulation box containing the crystal of copper was taken greater than the size of the DFZ to enable emitted dislocations to remain with this criterium within the simulation box.

The simulation sequence is then the following: the displacement on the outer boundary contour is applied corresponding to a given SIF. Each increment of the crack tip opening displacement corresponds to an increment of the SIF ΔK_I of $0.01 \text{ MPa}\cdot\sqrt{\text{m}}$ (see appendix A). Once the atoms inside the boundary condition zone (called external atoms) are displaced anisotropically, the other (called internal) are relaxed using a minimization algorithm in LAMMPS [41]. The convergence of the results was studied with two minimization algorithms available in LAMMPS (Conjugate Gradient and Fire) up to the desired precision. A CG algorithm was chosen with a threshold of 10^{-10} for these simulations. After the external atoms of the boundary condition zone were displaced according to the anisotropic profile, they are frozen and the rest of the crystal is relaxed with the CG minimization algorithm. The reason for that procedure is that usually, the part held frozen is the external boundary of the crystal [17]. However if only this procedure is followed, only one dislocation can be emitted before the crystal breaks at the boundary interface where every external atoms are frozen in place under the local stress concentration of the emitted dislocation. To avoid this problem that limits the number of dislocation emissions that one can study, every few steps the atoms inside the crystal (the internal atoms) were frozen and the external atoms were relaxed, so that the dislocations can exit the crystal. This creates a step at the outer boundary surface when exiting the crystal. This has allowed the simulations to go up to a large crack tip opening. The crack tip position is recalculated between each SIF increment to account for its change for the next computation of the anisotropic external displacement.

The behaviour at the crack tip is very dependent on the local configuration for an alloy. For the same concentration of zinc but a different alloy configuration, one obtains different results depending on the new crack tip solute configuration and local concentration. In this case, one could rely on a statistical approach by testing a large number of solute configurations. To reduce drastically the computational challenge, one can instead use the technique of a mean potential following Varvenne *et al* [58]. The mean potential is an EAM potential in which we consider only one type of atom for an alloy. The atomic potential is then a mix

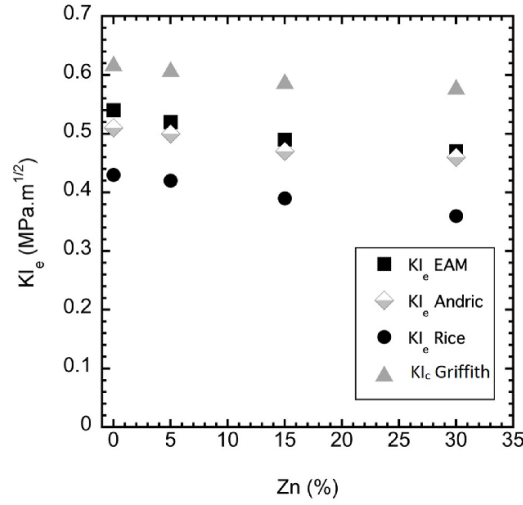


Figure 14. K_{Ic} for alpha-brass depending on zinc concentration.

(at the right composition) of the atoms potential in proportion of the alloy concentration. This type of potential allows one to run a simulation in which the result compares well with the mean of the results one would observe by running sufficient simulation at a given composition with different configurations as shown by Varvenne *et al* [58]. The use of this potential was first tested on already computed quantities such as elastic constants, stacking fault energies, lattice parameters and surface energies. The results found were sufficiently close to the mean of our numerous simulations enabling us to reduce drastically the computational burden of estimating the critical SIF for dislocation emission at the crack tip (more details can be found in appendix C).

5.2. Results

The SIFs for dislocation emission were simulated for α -brasses with zinc concentration up to 30% with the use of mean potential. They are shown on figure 14 along with the SIFs obtained with the theoretical calculations using the Peierls-Nabarro approach and adapted for the brass alloys introduced by Rice [15], and Andric and Curtin [17]. In addition the theoretical SIF for fracture as defined by Griffith [56] is given. In equation (B.3), the SIF depends on the energy release rate for a monocrystal G_{Ic} and a geometrical factor. Like Rice formulation, Andric formulation takes into account the USF energy, γ_{usf} . However, a surface energy term γ_s extending Schoeck's work [59] is included, taking into account that a surface step is created at the crack tip when a dislocation is emitted [17, 59].

The first point that can be observed from figure 14, is that the dislocation emission critical SIF is always below the Griffith fracture critical SIF. Dislocation emission conditions are reached before fracture. The new potential then predict a ductile behaviour of alpha-brass at every zinc concentration in this orientation in the traditional wisdom of a brittle to ductile transition driven by the crack tip emission of a dislocation. This behaviour is of course in line with the generic experimental ductile behaviour of α -brass. As stated in appendix B, there are

two different ways to compute the SIF for the first dislocation emission. The Rice approach in an anisotropic setup [15] or the Andric one [17] with a surface correction term induced by the dislocation emission. As can be seen on figure 14, where the data using both equations have been plotted, the Andric parametrization reproduces well the atomic simulations. This indicates that this parametrization incorporates correctly the effect of the creation of a surface step and can be used in other system than initially designed for in order to predict dislocation emission SIF. It fits very well the behaviour of the dislocation emission at the crack tip under anisotropic displacement conditions for our new CuZn alloy potential. As seen in figure 10, γ_{usf} is decreasing with the zinc concentration. Consequently, K_{Ie} decreases with the zinc concentration. That behaviour is well reproduced using the mean potential (as seen on figure 14).

5.3. Discussion

The results presented here show that the dislocation emission follows the relationship found by Andric *et al* for fcc pure elements (here for copper) [17] with a parametric dependance on the USF energy γ_{usf} and the surface energy γ_s . It is interesting to compare the new potential for copper for dislocation emission with the Mishin one. The γ_{usf} are different and the resulting K_{Ie} are different too. Nevertheless, the empirical relationship for K_{Ie} proposed by Andric *et al* captures equally well the variation both in γ_{usf} and γ_s . It was also applied by Andric *et al* to an alloy ($\text{Fe}_{1-x}\text{Ni}_{1-x}\text{Cr}_{2x}$) using the same relationship. In the FeNiCr alloy, there is a peak in the lattice parameter at 10%Cr. This peak is then repercut in the γ_{usf} evolution with solvent concentration [60]. The atomic simulations for the K_{Ie} reflects this change around 10%Cr with first an increase of the K_{Ie} with the concentration followed by a decrease beyond that threshold. The trend is different in our case where the misfit in lattice parameter due to solutes gives a strictly decreasing γ_{usf} (seen on figure 10), which in turn concurs to produce a strictly decreasing K_{Ie} . Andric *et al* relationship works correctly in our case as well for the Cu–Zn alloy. Concerning the decrease of K_{Ie} with alloying, we note the apparent contradiction between solid solution hardening and the lowering of K_{Ie} with alloying. One would not expect this behaviour since the α -brass alloy shows a solid solution hardening behaviour [61], meaning that the CRSS increases with the zinc concentration. However, this is in direct correlation with the decrease of the γ_{usf} with the zinc concentration. This shows that dislocation emission could be eased by alloying element showing a counterintuitive effect for dislocation emission at a crack tip in opposition to solute hardening. One can understand this effect by recalling that after emission while inside the bulk, the dislocation will be pinned to solute areas, introducing barriers for the movement of the dislocation requiring higher shear stresses to overcome. A resulting wavy conformation will appear giving rise to a line tension contribution all in all leading to hardening. The dislocation emission at a crack tip per se seems not to follow the solid solution hardening rule such that it appears as totally different processes. Further studies are planned on this point.

6. Conclusion

A new EAM potential was developed for copper and copper–zinc alloys that is meant to be used with α -brass up to 37% of zinc. It gives a good description for basic physical properties based on DFT such as cohesion (lattice constant and cohesive energy), elasticity (elastic constants) and plasticity (stacking faults, dislocation emission). For the CuZn alloy potential,

it was fitted to the DO_{23} (Cu_3Zn) ground state (DO_{23} for Cu_3Zn) for the alpha-brass and it correctly describes lattice constants and cohesive energies (mixing enthalpy) as a function of zinc concentration up to 30%. A basic study of the edge dislocation was carried out by computing the stacking fault energies (unstable and intrinsic) and the dissociation length. The atomic simulations reproduce well the elastic theory for the dislocation dissociation length. Moreover, the dislocation emission at a crack tip has been studied for different compositions of zinc. The results show good agreement with the theory incorporating a surface step creation at the crack tip when a dislocation is emitted. The emission of a dislocation at a crack tip is easier with alloying (decrease of the critical SIF with a greater concentration of zinc). It means that for a CuZn alloy, a dislocation is more easily emitted at the crack tip while it is to be pinned by solute elements leading to solid solution hardening. This is to be contrasted with the fact that for pure element the dislocation is emitted at a greater SIF but glide more easily in the crystal.

The Peierls stress for copper is comparable with experimental results, a detailed study of solid solution hardening versus dislocation emission process in α -CuZn alloys is left for a future study.

This EAM potential is shown to be well suited to model plasticity and fracture in α -brass alloys. This new EAM potential, since fitted on DFT results, can be used in a QM/MM framework based on DFT-GGA, with little correction required, increasing the possibilities of such simulations. In such framework, one may model with DFT the core of the defect (dislocation or crack tip) while the surrounding MM much larger volume is to be modelled with an interatomic potential (here EAM) [62]. Such a potential for copper and copper–zinc fcc alloys therefore opens the way to multi-scale modelling with this model material for various processes, such as studies of plasticity and fracture.

Data availability statement

All data that support the findings of this study are included within the article (and any supplementary files).

Acknowledgments

Funding from the French Agence nationale de la recherche (ANR) under the Project ANR Gauguin (No. ANR-18-CE08-0009-01) is gratefully acknowledged. This work was partly performed using HPC resources from Genci-IDRIS (Grant 2021-A0100912427). The authors acknowledge the use of the Cassiopee Arts et Métiers Institute of Technology HPC Center made available for conducting part of the research reported in this paper

Appendix A. Anisotropic boundary conditions

The stress intensity factors (SIFs) are computed with anisotropic boundary conditions. The crack is loaded by imposing a displacement on outer atoms in the crystal. These displacements are calculated using anisotropic fields based on the Stroh formalism [57]. Since we examine the crack tip dislocation emission in pure mode I, the increment of displacement is an increment in the SIF of this mode and is given by:

$$\begin{cases} \Delta u_x = \Delta K_I \sqrt{\frac{2r}{\pi}} \operatorname{Re} \left(\frac{1}{a_1 - a_2} (a_1 p_2 \sqrt{\cos \theta + a_2 \sin \theta} - a_2 p_1 \sqrt{\cos \theta + a_1 \sin \theta}) \right) \\ \Delta u_y = \Delta K_I \sqrt{\frac{2r}{\pi}} \operatorname{Re} \left(\frac{1}{a_1 - a_2} (a_1 q_2 \sqrt{\cos \theta + a_2 \sin \theta} - a_2 q_1 \sqrt{\cos \theta + a_1 \sin \theta}) \right) \end{cases} \quad (\text{A.1})$$

In equation (A.1), p_1, p_2, q_1, q_2 are given by the following set of equations:

$$\begin{cases} p_1 = S_{11}^p a_1^2 + S_{12}^p - S_{16}^p a_1 \\ p_2 = S_{11}^p a_2^2 + S_{12}^p - S_{16}^p a_2 \\ q_1 = S_{12}^p a_1 + \frac{S_{22}^p}{a_1} - S_{26}^p \\ q_2 = S_{12}^p a_2 + \frac{S_{22}^p}{a_2} - S_{26}^p a_2. \end{cases} \quad (\text{A.2})$$

With a_1 and a_2 the roots with a positive imaginary part of the following equation:

$$S_{11}^p a^4 - 2S_{16}^p a^3 + (2S_{12}^p + S_{66}^p) a^2 - 2S_{26}^p a + S_{22}^p = 0. \quad (\text{A.3})$$

With $S_{ij}^p = S_{ij} - \frac{S_{i3} S_{3j}}{S_{33}}$ with S the compliance matrix. The other roots are the complex conjugate of a_1 and a_2 .

With this imposed displacement, the stress imposed in the crystal in polar coordinates then reads:

$$\begin{cases} \sigma_{11} = \frac{K_I}{\sqrt{2\pi r}} \operatorname{Re} \left(\frac{a_1 a_2}{a_1 - a_2} \left(\frac{a_2}{\sqrt{\cos \theta + a_2 \sin \theta}} - \frac{a_1}{\sqrt{\cos \theta + a_1 \sin \theta}} \right) \right) \\ \sigma_{22} = \frac{K_I}{\sqrt{2\pi r}} \operatorname{Re} \left(\frac{1}{a_1 - a_2} \left(\frac{a_1}{\sqrt{\cos \theta + a_2 \sin \theta}} - \frac{a_2}{\sqrt{\cos \theta + a_1 \sin \theta}} \right) \right) \\ \sigma_{12} = \frac{K_I}{\sqrt{2\pi r}} \operatorname{Re} \left(\frac{a_1 a_2}{a_1 - a_2} \left(\frac{1}{\sqrt{\cos \theta + a_1 \sin \theta}} - \frac{1}{\sqrt{\cos \theta + a_2 \sin \theta}} \right) \right) \end{cases} \quad (\text{A.4})$$

with $K_I \in \mathbb{R}$.

Appendix B. Anisotropic geometric factors

The theoretical values of the first partial dislocation emission have been calculated with Rice criterion [15]:

$$K_{Ie} = \sqrt{\frac{2\mu\gamma_{usf}}{1-\nu}} \frac{1}{\cos^2 \frac{\theta}{2} \sin \frac{\theta}{2}} \quad (\text{B.1})$$

but modified by Sun and Beltz [16] for anisotropic crystals:

$$K_{Ie} = \sqrt{\gamma_{usf} \mathcal{O}(\theta, \phi)} \frac{1}{F_{12}(\theta)} \quad (\text{B.2})$$

and further modified by Andric and Curtin [17] to take into account the small step created by the emission of the dislocation:

$$K_{Ie} = \sqrt{G_{Ie} \mathcal{O}(\theta, \phi)} \frac{1}{F_{12}(\theta)}. \quad (\text{B.3})$$

Here $G_{Ie} = 0.145\gamma_s + 0.5\gamma_{usf}$, θ is the angle between the crack tip and the slip plane and ϕ the angle between the dislocation Burgers vector and the crack front direction. The F_{12} factor is a geometrical factor that depends only on the angle θ and the compliance matrix of the material.

The F_{ij} are calculated using the stress field induced by an anisotropic displacement at an angle θ between the crack tip and the slip plane of the dislocation.

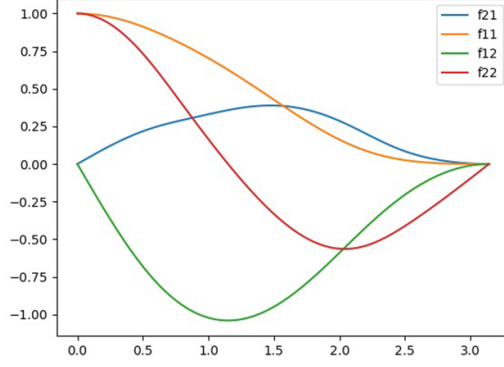


Figure B1. F_{ij} for copper with the new potential.

The matrix F is the angular distribution of the stress at the crack tip [17]. It can be written as:

$$F = \Omega(\theta)\sigma\Omega^T(\theta) \quad (\text{B.4})$$

with Ω the rotation matrix

$$\Omega(\theta) = \begin{bmatrix} \cos\theta & \sin\theta \\ -\sin\theta & \cos\theta \end{bmatrix}$$

and σ the stress matrix with σ_{11} , σ_{12} and σ_{22} as defined in equation (A.4)

$$\sigma = \begin{bmatrix} \sigma_{11} & \sigma_{12} \\ \sigma_{12} & \sigma_{22} \end{bmatrix}.$$

These F_{ij} were computed depending on the theta angle for copper with this potential and they are plotted on figure B1. The F_{ij} correspond to different coefficients for mode I and II or mixed loading. In mode I loading, one is interested into F_{12} .

Appendix C. Mean potential

The EAM potential was meaned as in [58] in view of using it for the dislocation emission process at a crack tip for CuZn alloys. In order to validate the approach in our case, it was compared to the EAM potential used for different configurations. It was compared for elastic constants in figure C1 and stacking fault energies in figure C2. As can be seen in figure C1, the elastic constants computed with the mean EAM potential compare well (up to 20%) with the atomic Cu–Zn EAM potential used with different configurations. A discrepancy appears above 25% but the disagreement remains below 10% for the elastic constants.

It was then used to compute the stacking fault energies (both unstable and intrinsic). As can be seen on figure C2, the stacking fault energies computed with the mean potential stays in the error margin of the stacking fault energies computed with 100 configurations with the EAM potential.

As seen on both figures, the mean EAM potential reproduces well the interactions reproduced by the EAM potential. However it cannot be used for dislocation glide studies in α -brass. The α -brass alloy CRSS is supposed to increase with the zinc concentration due to pinning the dislocation by solute atoms while here the USF decreases with alloying. With the mean EAM potential, there are no more varying local concentration of solute atoms so while the source of an increase of CRSS stems from the wavy local shape of the dislocation core, this process cannot be modelled using meaned potentials because the core remains straight.

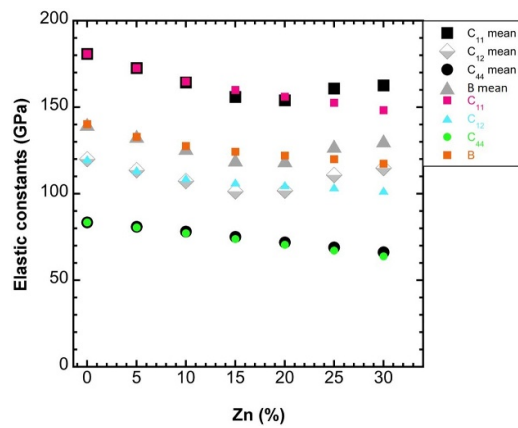


Figure C1. Elastic constants in alpha-brasses with the new EAM potential and the mean one.

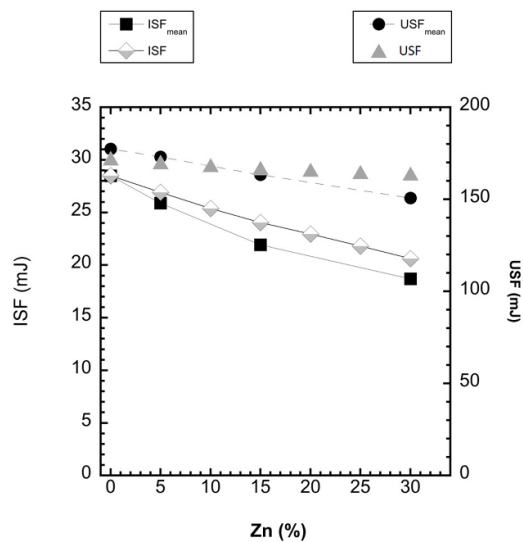


Figure C2. Stacking fault energies in alpha-brasses with the new EAM potential and the mean one.

ORCID iD

Thierry Auger  <https://orcid.org/0000-0002-2338-599X>

References

- [1] Madelung O (ed) 1994 Cu-Zn Cr-Cs—Cu-Zr (*Landolt-Börnstein—Group IV Physical Chemistry*) vol 5d (Berlin: Springer)
- [2] Cai J and Ye Y Y 1996 Simple analytical embedded-atom-potential model including a long-range force for fcc metals and their alloys *Phys. Rev. B* **54** 8398–410

- [3] Mishin Y, Mehl M J, Papaconstantopoulos D A, Voter A F and Kress J D 2001 Structural stability and lattice defects in copper: *ab initio*, tight-binding and embedded-atom calculations *Phys. Rev. B* **63** 224106
- [4] Kang K-H, Sa I, Lee J-C, Fleury E and Lee B-J 2009 Atomistic modeling of the Cu–Zr–Ag bulk metallic glass system *Scr. Mater.* **61** 801–4
- [5] Wadley H N G, Zhou X, Johnson R A and Neurock M 2001 Mechanisms, models and methods of vapor deposition *Prog. Mater. Sci.* **46** 329–77
- [6] Sieradzki K and Newman R C 1987 Stress-corrosion cracking *J. Phys. Chem. Solids* **48** 1101–13
- [7] Nichols H and Rostoker W 1961 On the mechanism of crack initiation in embrittlement by liquid metals *Acta Metall.* **9** 504–9
- [8] Nichols H and Rostoker W 1960 Ductile-brittle transition in alpha-brass *Acta Metall.* **8** 848–50
- [9] Mitchell T E and Thornton P R 1963 The work-hardening characteristics of Cu and alpha-brass single crystals between 4.2 and 500 °K *Phil. Mag. A* **8** 1127–59
- [10] Dickel D E, Baskes M I, Aslam I and Barrett C D 2018 New interatomic potential for Mg–Al–Zn alloys with specific application to dilute Mg-based alloys *Modelling Simul. Mater. Sci. Eng.* **26** 045010
- [11] Rodary E, Rodney D, Proville L, Bréchet Y and Martin G 2004 Dislocation glide in model Ni(Al) solid solutions by molecular dynamics *Phys. Rev. B* **70** 054111
- [12] Liu X-Y, Ohotnicky P P, Adams J B, Rohrer C L and Hyland R W 1997 Anisotropic surface segregation in Al–Mg alloys *Surf. Sci.* **373** 357–70
- [13] Patinet S and Proville L 2008 Depinning transition for a screw dislocation in a model solid solution *Phys. Rev. B* **78** 104109
- [14] Patinet S and Proville L 2011 Dislocation pinning by substitutional impurities in an atomic-scale model for Al(Mg) solid solutions *Phil. Mag.* **91** 1581–606
- [15] Rice J R 1992 Dislocation nucleation from a crack tip: an analysis based on the Peierls concept *J. Mech. Phys. Solids* **40** 239–71
- [16] Sun Y and Beltz G E 1994 Dislocation nucleation from a crack tip: a formulation based on anisotropic elasticity *J. Mech. Phys. Solids* **42** 1905–32
- [17] Andric P and Curtin W A 2017 New theory for Mode I crack-tip dislocation emission *J. Mech. Phys. Solids* **106** 315–37
- [18] Daw M S and Baskes M I 1984 Embedded-atom method: derivation and application to impurities, surfaces and other defects in metals *Phys. Rev. B* **29** 6443–53
- [19] Banerjee A and Smith J R 1988 Origins of the universal binding-energy relation *Phys. Rev. B* **37** 6632–45
- [20] Johnson R A 1989 Alloy models with the embedded-atom method *Phys. Rev. B* **39** 12554–9
- [21] Bonny G, Pasianot R C and Malerba L 2009 Fitting interatomic potentials consistent with thermodynamics: Fe, Cu, Ni and their alloys *Phil. Mag.* **89** 3451–64
- [22] Gola A and Pastewka L 2018 Embedded atom method potential for studying mechanical properties of binary Cu–Au alloys *Modelling Simul. Mater. Sci. Eng.* **26** 055006
- [23] Turchi P E A, Sluiter M, Pinski F J, Johnson D D, Nicholson D M, Stocks G M and Staunton J B 1991 First-principles study of phase stability in Cu–Zn substitutional alloys *Phys. Rev. Lett.* **67** 1779–82
- [24] Müller S and Zunger A 2001 Structure of ordered and disordered alpha-brass *Phys. Rev. B* **63** 094204
- [25] Kresse G and Hafner J 1993 *Ab initio* molecular dynamics for liquid metals *Phys. Rev. B* **47** 558–61
- [26] Kresse G and Hafner J 1994 *Ab initio* molecular-dynamics simulation of the liquid-metal-amorphous-semiconductor transition in germanium *Phys. Rev. B* **49** 14251–69
- [27] Kresse G and Furthmüller J 1996 Efficiency of *ab-initio* total energy calculations for metals and semiconductors using a plane-wave basis set *Comput. Mater. Sci.* **6** 15–50
- [28] Kresse G and Furthmüller J 1996 Efficient iterative schemes for *ab initio* total-energy calculations using a plane-wave basis set *Phys. Rev. B* **54** 11169–86
- [29] Perdew J P, Burke K and Ernzerhof M 1996 Generalized gradient approximation made simple *Phys. Rev. Lett.* **77** 3865–8
- [30] Perdew J P, Burke K and Ernzerhof M 1997 Generalized gradient approximation made simple [Phys. Rev. Lett. 77, 3865 (1996)] *Phys. Rev. Lett.* **78** 1396
- [31] Blöchl P E 1994 Projector augmented-wave method *Phys. Rev. B* **50** 17953–79
- [32] Kresse G and Joubert D 1999 From ultrasoft pseudopotentials to the projector augmented-wave method *Phys. Rev. B* **59** 1758–75

- [33] Nelder J A and Mead R 1965 A simplex method for function minimization *Comput. J.* **7** 308–13
- [34] Larsen A H *et al* 2017 The atomic simulation environment—a Python library for working with atoms *J. Phys.: Condens. Matter* **29** 273002
- [35] Foiles S M, Baskes M I and Daw M S 1986 Embedded-atom-method functions for the fcc metals Cu, Ag, Au, Ni, Pd, Pt and their alloys *Phys. Rev. B* **33** 7983–91
- [36] Kittel C 2005 *Introduction to Solid State Physics* 8th edn (Hoboken, NJ: Wiley)
- [37] Giri A K and Mitra G B 1985 Extrapolated values of lattice constants of some cubic metals at absolute zero *J. Phys. D: Appl. Phys.* **18** L75–L78
- [38] Dal Corso A, Pasquarello A and Baldereschi A 1997 Density-functional perturbation theory for lattice dynamics with ultrasoft pseudopotentials *Phys. Rev. B* **56** R11369–72
- [39] Alfè D 2009 PHON: a program to calculate phonons using the small displacement method *Comput. Phys. Commun.* **180** 2622–33
- [40] Nilsson G and Rolandson S 1973 Lattice dynamics of copper at 80 K *Phys. Rev. B* **7** 2393–400
- [41] Plimpton S 1995 Fast parallel algorithms for short-range molecular dynamics *J. Comput. Phys.* **117** 1–19
- [42] Orr R L and Argent B B 1965 Heats of formation of alpha-brass *Trans. Faraday Soc.* **61** 2126–31
- [43] Kowalski M and Spencer P J 1993 Thermodynamic reevaluation of the Cu–Zn system *J. Phase Equilib.* **14** 432–8
- [44] Rao S S and Anantharaman T R 1963 Accurate evaluation of lattice parameters of alpha-brasses *Curr. Sci.* **32** 262–3 (available at: www.jstor.org/stable/24214179)
- [45] Johnson D D, Nicholson D M, Pinski F J, Györffy B L and Stocks G M 1990 Total-energy and pressure calculations for random substitutional alloys *Phys. Rev. B* **41** 9701–16
- [46] Rayne J A 1959 Elastic constants of α -brasses: room-temperature variation with solute concentration *Phys. Rev.* **115** 63–66
- [47] Pettifor D G 1995 *Bonding and Structure of Molecules and Solids* (Oxford: Clarendon, Oxford University Press)
- [48] Li W, Lu S, Hu Q M, Kwon S K, Johansson B and Vitos L 2014 Generalized stacking fault energies of alloys *J. Phys.: Condens. Matter* **26** 265005
- [49] Howie A and Swann P R 1961 Direct measurements of stacking-fault energies from observations of dislocation nodes *Phil. Mag.* **6** 1215–26
- [50] Gallagher P C J 1970 The influence of alloying, temperature and related effects on the stacking fault energy *Metall. Mater. Trans. B* **1** 2429–61
- [51] Wu X-Z, Wang R, Wang S-F and Wei Q-Y 2010 *Ab initio* calculations of generalized-stacking-fault energy surfaces and surface energies for FCC metals *Appl. Surf. Sci.* **256** 6345–9
- [52] Hirth J P and Lothe J 1982 *Theory of Dislocations* 2nd edn (New York: Wiley)
- [53] Weiler B, Sigle W and Seeger A 1995 High-resolution electron-microscopy study of 60°-Dislocations in Cu *Phys. Status Solidi a* **150** 221–5
- [54] Aslanides A and Pontikis V 1998 Atomistic study of dislocation cores in aluminium and copper *Comput. Mater. Sci.* **10** 401–5
- [55] Kamimura Y, Edagawa K and Takeuchi S 2013 Experimental evaluation of the Peierls stresses in a variety of crystals and their relation to the crystal structure *Acta Mater.* **61** 294–309
- [56] Griffith A A 1921 VI. The phenomena of rupture and flow in solids *Phil. Trans. R. Soc. A* **221** 163–98
- [57] Stroh A N 1957 A theory of the fracture of metals *Adv. Phys.* **6** 418–65
- [58] Varvenne C, Luque A, Nöhning W G and Curtin W A 2016 Average-atom interatomic potential for random alloys *Phys. Rev. B* **93** 104201
- [59] Schoeck G 2003 The emission of dislocations from crack tips *Mater. Sci. Eng. A* **356** 93–101
- [60] Andric P 2019 The mechanics of crack-tip dislocation emission and twinning *PhD Thesis* Ecole Polytechnique Fédérale de Lausanne
- [61] Feltham P 1968 Solid solution hardening of metal crystals *J. Phys. D: applied physics* **1** 303–8
- [62] Bernstein N, Kermode J R and Csányi G 2009 Hybrid atomistic simulation methods for materials systems *Rep. Prog. Phys.* **72** 026501